Princeton Plasma Physics Laboratory

PPPL-

PPPL-

Princeton Plasma Physics Laboratory
Report Disclaimers

PPPL Report Availability

Princeton Plasma Physics Laboratory:

http://www.pppl.gov/techreports.cfm

Office of Scientific and Technical Information (OSTI):

http://www.osti.gov/bridge

Related Links:

U.S. Department of Energy

Office of Scientific and Technical Information

Fusion Links

Properties of Alfvén Eigenmodes in the TAE range on the National Spherical Torus Experiment-Upgrade

M. Podestà, N. N. Gorelenkov, R. B. White, E. D. Fredrickson, S. P. Gerhardt and G. J. Kramer

Princeton Plasma Physics Laboratory, Princeton NJ 08543 - USA

(Dated: April 22, 2013)

A second Neutral Beam (NB) injection line is being installed on the NSTX Upgrade device, resulting in six NB sources with different tangency radii that will be available for heating and current drive. This work explores the properties of instabilities in the frequency range of the Toroidal Alfvén Eigenmode (TAE) for NSTX-U scenarios with various NB injection geometries, from more perpendicular to more tangential, and with increased toroidal magnetic field with respect to previous NSTX scenarios. Predictions are based on analysis through the ideal MHD code NOVA-K. For the scenarios considered in this work, modifications of the Alfvén continuum result in a frequency up-shift and a broadening of the radial mode structure. The latter effect may have consequences for fast ion transport and loss. Preliminary stability considerations indicate that TAEs are potentially unstable, with ion Landau damping representing the dominant damping mechanism.

I. INTRODUCTION

The NSTX spherical torus (ST) [1] is presently undergoing a major upgrade (NSTX-U [2]), whose main elements are the enhancement of the center column and the installation of a second neutral beam (NB) injection line. The upgraded center column will enable longer plasma discharges, up to $\sim$ 5 seconds, and a doubling in the toroidal field and plasma current, up to $B_t = 1$ T and $I_p = 2$ MA, respectively. The second NB line is aimed at more tangential injection of fast neutrals with respect to the existing NB system (Fig. 1), thus providing more flexibility for the optimization of NB-driven current. Each NB line is composed of 3 sources with different tangency radius, R_{tan}. Maximum injection energy is $E_{inj} = 95$ keV, with up to 14 MW of total NB power available.

Efficient and well-controlled NB current drive is of particular relevance for NSTX-U and STs in general, in view of the design of devices such as a future Fusion Nuclear Science Facility based on the ST concept [3]. Because of their compact size, those devices are likely to operate without a central solenoid and will heavily rely on non-inductive current drive for both current ramp-up and sustainment in the steady-state phase. Discharge optimization toward high performance on NSTX-U and future devices requires a precise knowledge of the NB driven current, especially when the behavior of the injected NB ions deviates from classical predictions. This can happen when fast ion driven instabilities in the frequency range of the Toroidal Alfvén Eigenmode (TAE) cause fast ion redistribution, thus affecting the NB driven current. From previous studies, it is well known that TAEs can efficiently interact with NB ions [4][5], leading to loss or redistribution of fast particles [6][7][8][9]. The resulting NB-driven current profile can deviate considerably from what predicted if fast ions behaved classically [10][11].

As the NSTX Upgrade proceeds toward completion, with the first plasma planned by the end of 2014, it is therefore important to investigate what the expected scenarios will be and how they can be improved or
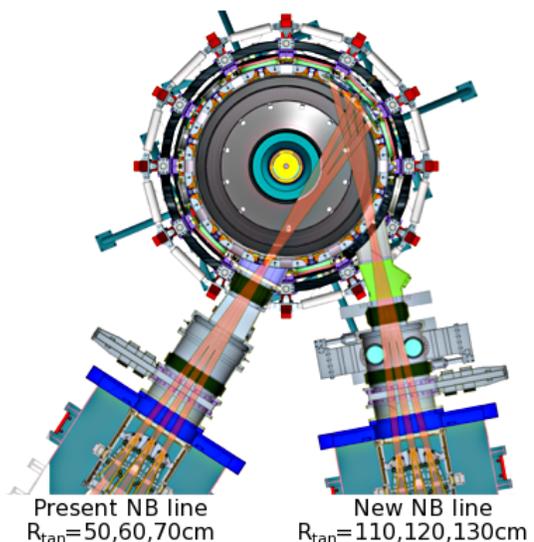

FIG. 1. (Color online) Elevation of NSTX-U showing the present NB line and the 2nd (new, more tangential) NB line. Each NB line includes 3 sources with different tangency radii.

optimized. This work focuses on the expected properties of low-frequency AEs, namely TAEs (and, indirectly, Reverse-shear AEs - RSAEs) and Ellipticity-induced AEs, in the steady-state phase of H-mode NSTX-U plasmas. The two main goals are: (i) to investigate if - and how - AE properties change with respect to NSTX scenarios; (ii) to assess variations of AE properties as a function of the NB injection geometry, e.g. of the combination of NB sources with different tangency radii. Projections of AE properties as a function of other parameters, such as the safety factor profile and plasma density and temperature, are deferred to future studies.

The main tool for AE analysis is the ideal MHD code NOVA, complemented by a kinetic post-processor for computation of AE stability (NOVA-K) [12][13]. The analysis shows that NSTX-U scenarios studied herein
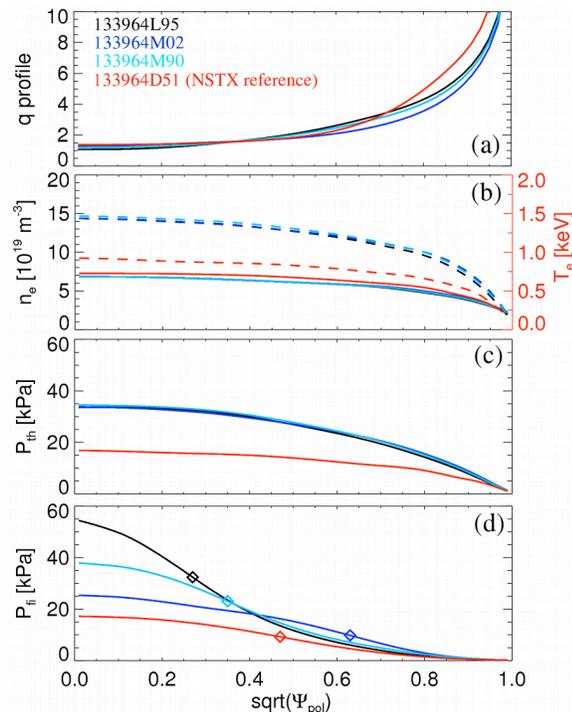
FIG. 2. (Color online) NSTX-U profiles used in this study. On the abscissa is the square root of the poloidal flux, normalized to its value at the edge, that roughly coincides with the normalized minor radius coordinate. (a) Safety factor. (b) Electron density (solid) and temperature (dashed). (c) Thermal plasma pressure. (d) Fast ion pressure. Diamonds indicate the radius of steepest fast ion pressure gradient. In all panels, curves in red refer to the reference NSTX scenario.

have broader TAE gaps, hence potentially broader mode structures, than the reference NSTX case. An up-shift of the spectrum of the most unstable modes is also expected, with toroidal mode numbers in the range $n = 2 - 8$. One important conclusion is the sensitivity of the results on toroidal rotation, v_ϕ, with a net contraction of the AE gaps with respect to the $v_\phi = 0$ case. In fact, the local AE frequency is usually comparable to, or even smaller than, the Doppler shift frequency. Although fully self-consistent stability calculations for these fast spinning plasmas are still out of reach for the NOVA-K code, the approximate treatment used in this work captures the main effects of large rotation on mode structure and stability.

The remainder of the paper is organized as follows. The scenarios examined in this work are introduced in Sec. II. Section III presents the general properties of the AE gaps in the TAE range of frequency and compares NSTX to NSTX-U predicted scenarios. More detailed analysis of the mode structure and stability is discussed in Sec. IV and V, respectively. Section VI summarizes the main results of this work and concludes the paper.

case ID	R_{tan} [cm]	E_{inj} [keV]	$B_t(0)$ [kG]	I_p [MA]
D51	50,60,70	90,90,90	5	0.7
M90	50,60,70	90,90,90	8	1
M02	50,60,130	90,90,95	8	1
L95	50,60,110	90,90,95	8	1

TABLE I. Run identifiers and main parameters of the 4 cases studied in this work. All simulations are based on the same NSTX discharge #133964.

II. NSTX-U SCENARIOS

NSTX-U is a spherical torus with major and minor radius $R_0 = 0.9$ m and $a = 0.65$ m (aspect ratio $R_0/a \approx 1.4-1.6$). For the analyses discussed herein, the magnetic field is $5 - 8$ kG, with the former corresponding to the reference NSTX discharge. Values > 5 kG refer to the predicted NSTX-U scenarios. The plasma current is $I_p = 0.7 - 1$ MA. Density and temperature are $n_e \approx 7 \times 10^{19}$ m^{-3} and $T_i \approx T_e \leq 0.8 - 1.5$ keV (subscripts e, i refer to electrons and ions, respectively, see Fig. 2b). All cases represent H-mode confinement regimes.

For this study, three NSTX-U scenarios with monotonic safety factor profile have been selected from the comprehensive database examined in Ref. [14]. Main parameters are shown in Fig. 2 and summarized in Tab. I. The three cases present very similar equilibrium profiles, except for the fast ion pressure resulting from NB injection with different combinations of the available NSTX-U sources. The mix of NB sources is summarized in Tab. I. Two of the sources that were already available on NSTX provide a baseline power of 4 MW with tangency radii of 50 and 60 cm and injection energy 90 keV. A third source is used to modify the overall deposition profile. The tangency radius varies from 70 cm (NSTX-like case) to 110 and 130 cm. The latter values correspond to nearly tangential injection (the magnetic axis is at ≈ 105 cm) and to off-axis injection at the outboard plasma, respectively. The toroidal field is $B_t \simeq 8$ kG, which is the expected maximum value that will be achievable during the initial year of NSTX-U operation. NSTX-U scenarios are compared with a reference NSTX case with $B_t = 5$ kG.

III. GENERAL FEATURES OF ALFVÈN EIGENMODES GAPS IN NSTX-U

Qualitative projections of the general AE properties from know NSTX scenarios to predicted NSTX-U conditions can be made on the basis of the AE gap structure dependence on global parameters, such as aspect ratio, toroidal field and density [5]. The gap center frequency, $f_{0,gap}$, scales as

$$f_{0,gap} \sim \frac{v_A}{4\pi q R_0} \sim \frac{B_t}{n_e^{1/2} q R_0} \qquad (1)$$
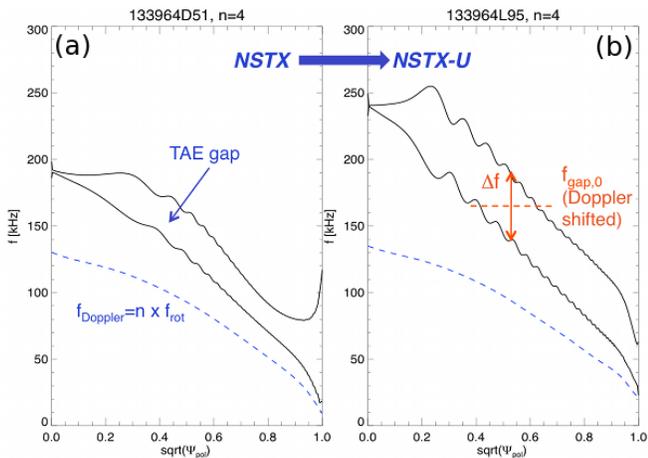
FIG. 3. (Color online) Comparison of TAE gaps for (a) NSTX and (b) NSTX-U scenarios.

FIG. 4. (Color online) Example of TAE gap modification when a large toroidal rotation is included in the analysis.

where $v_A \propto B_t/n_e^{1/2}$ is the Alfvén velocity and q the safety factor. Assuming that safety factor and density do not vary substantially for the equilibria considered herein, cf. Fig. 2, Eq. 1 implies a roughly linear scaling between typical AE frequencies and the toroidal field.

Similarly, the relative gap frequency width, $\Delta f_{0,gap}/f_{0,gap}$, depends on the relative variation of the magnetic field across the plasma [5]:

$$\frac{\Delta f_{0,gap}}{f_{0,gap}} \propto \frac{B_{max} - B_{min}}{\bar{B}} \tag{2}$$

with $\bar{B}$ the average magnetic field. The right-hand side in Eq. 2 is proportional to the inverse aspect ratio, which is only slightly reduced in NSTX-U. Therefore, the relative gap width remains nearly constant. In absolute terms, $\Delta f_{0,gap}$ is expected to increase linearly with $f_{0,gap}$.

Proceeding on the same line, modifications of the spectrum of most unstable (or least stable) modes can be estimated from the general condition for maximum wave-particle interaction [15], $k_\perp \rho_f \sim 1$, where $k_\perp$ is the perpendicular wave-vector of the mode and ρ_f the fast ion Larmor radius. By introducing the poloidal mode number m and the gyro-frequency $\omega_f = v_f/\rho_f$ for fast ion velocities v_f, the following relation is obtained:

$$k_\perp \rho_f \sim 1 \Rightarrow \frac{nq}{a} \frac{v_f}{\omega_f} \sim 1 \Rightarrow n \propto B \tag{3}$$

The approximations $k_\perp \sim m/a$ and $n \sim m/q$ have been used in Eq. 3. The dependence on minor radius and q have been dropped since those quantities remain, at first order, unchanged. In practice, Eq. 3 indicates that the spectrum of toroidal mode number for potentially unstable modes is expected to shift up proportionally to the magnetic field. Starting from typical toroidal mode numbers $n = 2 - 5$ of RSAEs and TAEs on NSTX, the two-fold increase in B_t on NSTX-U will favor modes with intermediate n's, up to $n \approx 8 - 10$.
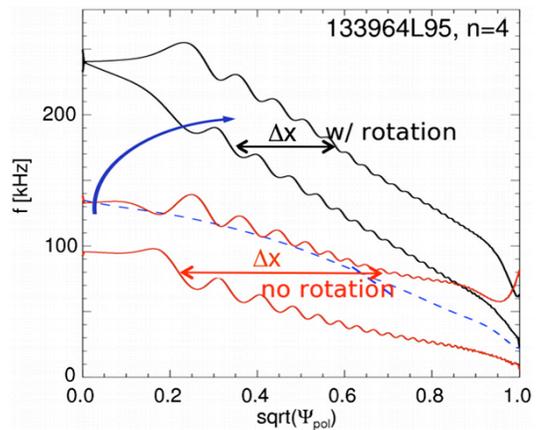
IV. NOVA ANALYSIS OF AE PROPERTIES

The general trends from Eqs. 1-2 are confirmed by analysis of the AE gap structure through the ideal MHD code NOVA [12][13]. Starting from each plasma equilibrium, NOVA is used to compute the gap structure and the resulting Alfvén eigenmodes. (Note that the radial coordinate $\Psi_{pol}^{1/2} \approx r/a$ is used throughout the remainder of the paper, with Ψ_{pol} being the poloidal flux normalized to its value at the last closed flux surface).

A first example is shown in Fig. 3, where the gap structure for $n = 4$ is shown for the reference NSTX case with $B_t = 5$ kG and for one of the NSTX-U scenarios with $B_t = 8$ kG. The qualitative features discussed above are recovered, with a general increase in the frequency of the TAE bottom and top continua and an overall increase in the frequency width of the TAE gap.

An important feature appears in Fig. 3, namely the large contribution of the Doppler shift, $f_{Doppler}$, caused by finite toroidal rotation, f_{rot}, to the AE frequency in the laboratory frame:

$$f_{AE} = f_{AE,plasma} + \underbrace{n \times f_{rot}}_{f_{Doppler}} \tag{4}$$

This is further illustrated in Fig. 4, where the continuum is computed for the same case as in Fig. 3b but setting the toroidal rotation to zero. In this case, the gap center frequency (hence, the frequency of the AE modes residing inside the gap) in the plasma frame is consistently lower than the Doppler shift contribution. This feature is quite unique for modes in the TAE frequency range observed in spherical torii with dominant auxiliary heating provided by NB injection and relatively low magnetic field (i.e. low $f_{AE,plasma}$). The large NB input torque concurs with the small aspect ratio to produce fast spin-up of the plasma, resulting in observed mode frequencies that are considerably higher than the expected mode frequency in the plasma frame. The implications for a reliable stability analysis are further discussed in Sec. V.
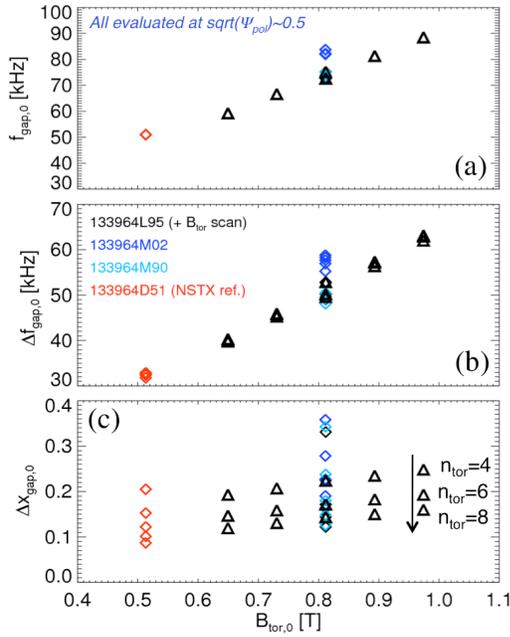
FIG. 5. (Color online) Modifications of the TAE gap properties as a function of toroidal field for mode numbers $n = 4-8$. (a) Central gap frequency. (b) Frequency width of the gap. (c) Radial width of the gap. Different scenarios are color-coded according to the legend in panel (b).
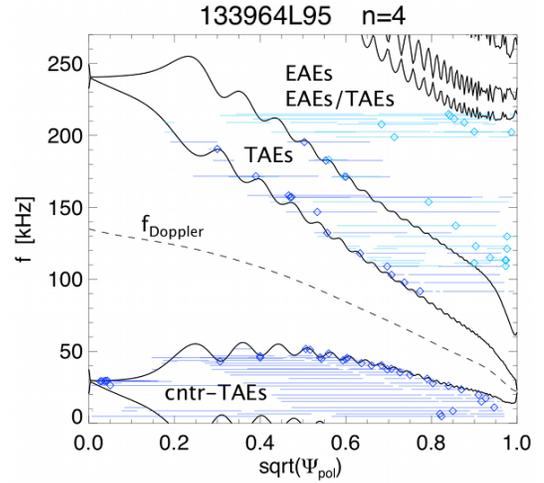

FIG. 6. (Color online) Continuum structure from NOVA for TAE and EAE modes for $n = 4$. Rotation is included. The mode search range is $0 - 50$ kHz and $70 - 220$ kHz. Dashed line indicates the Doppler shift frequency for $n = 4$, based on the toroidal rotation profile.

Besides the effects on f_{AE}, finite rotation also modifies the AE gaps to an extent not usually observed in conventional aspect ratio tokamaks. A direct consequence of this is the contraction of the *radial* AE gap width, Δx, for increasing f_{rot}, which is also evident from Fig. 4.

A more comprehensive verification of the predictions from Eqs. 1-2 is given in Fig. 5. All three NSTX-U scenarios, as well as the reference NSTX case, are included in the analysis. In addition, a toroidal field scan is performed starting from a NSTX-U case to cover the expected B_t range of operation for NSTX-U. Note that the toroidal field on axis is the only parameter that varies in the scan, whereas all the other profiles are kept constant.

The trends of $f_{0,gap}$ and $\Delta f_{0,gap}$ with B_t are confirmed. Moreover, the effects of plasma rotation on the radial gap width can be quantified for modes with different toroidal number. As n increases, the overall slope of the continuum moving from the center to the edge increases because of the larger Doppler shift, which is proportional to n. The net result is a radial compression of the gap, so that only narrower TAE modes will be found with respect to the $f_{rot} \equiv 0$ case. In practice, this can impose an upper limit to the observed spectrum of unstable modes (cf. Eq. 3), because very localized modes may not feed on a sufficiently large portion of the fast ion profile.

The analysis of the mode structure adds more important information to the AE predictions for NSTX-U. Figure 6 shows an overview of the Alfvén eigenmodes identified by NOVA in the frequency range $0 - 220$ kHz for a

NSTX-U H-mode scenario. In the selected range, three classes of modes are found:

i - Proper TAEs, with peak amplitude well inside the TAE gap.

ii - EAEs and mixed EAE/TAE modes in the ellipticity-induced gap.

iii - A second group of TAEs at low frequency. These TAEs are nominally residing in the *counter-propagating* TAE gap, which is turned to the co-going direction (in the laboratory frame) by the large Doppler shift.

Modes with very strong interaction with the continuum are excluded from the analysis. Similarly, a condition on the regularity of the mode structure is used to select plausible modes only. For instance, modes that peak at (or around) the radius where their frequency intercepts the continuum are removed from the set of valid solutions. A further selection is required because of the possibility for NOVA to find *degenerated* (i.e. multiple) solutions that have essentially the same radial structure, but slightly different frequencies (cf. Fig. 13 in Ref. [8]). Only one of the degenerated solutions is retained for further analysis.

Examples of mode structure for each class are illustrated in Fig. 7. While modes in class (i) are well-known and characterized, the mixed EAE/TAE modes in class (ii) are less commonly encountered in tokamak research and deserve additional comments. They present all the features reported in Ref. [16] for so-called *double-gap* Alfvén eigenmodes, i.e. AEs that can tunnel through the continuum without discontinuities and couple to a different AE type that resides in an adjacent AE gap. The interest for double-gap modes on NSTX-U is dictated by
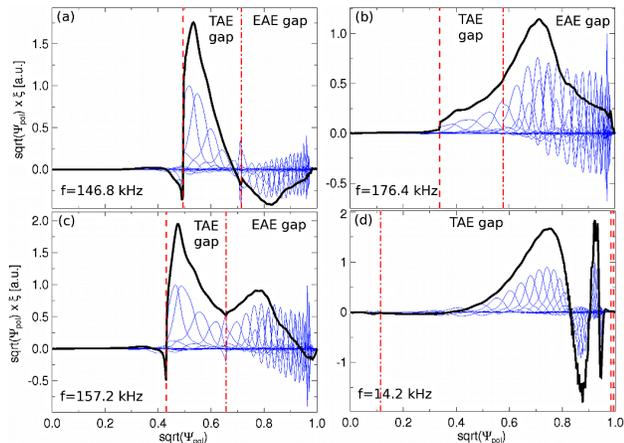
FIG. 7. (Color online) Examples of $n = 4$ AE mode structures from NSTX-U case $L95$ showing modes with predominant (a) TAE and (b) EAE character, along with (c) mixed TAE/EAE modes and (d) counter-propagating TAEs turned to $f > 0$ by the large Doppler-shift. Thin curves show single poloidal harmonics. The total mode structure is shown by the thick line. Vertical dashed (dash-dotted) lines indicate the intersection of the mode with the lower (upper) TAE continuum.
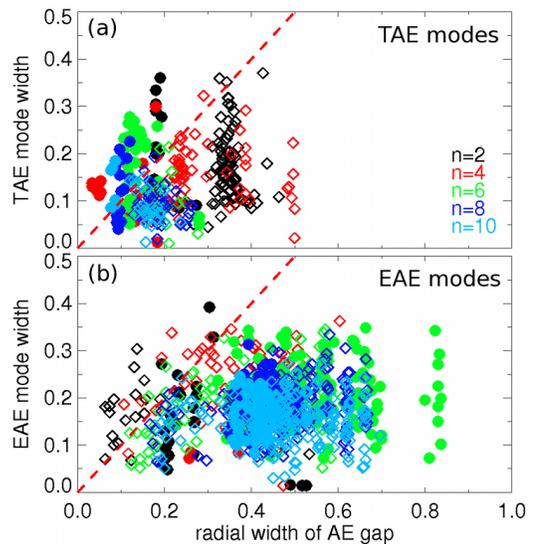

FIG. 8. (Color online) Effective radial mode width w_{mode} for (a) TAE and (b) EAE modes *vs.* radial gap width, based on NOVA analysis. Data from NSTX (NSTX-U) are shown as full (empty) symbols. Color coding of the different toroidal mode numbers is reported in panel (a). Dashed lines indicate where w_{mode} equals the gap width.

the possible consequences that inter-gap coupling can induce. Firstly, the modes span a considerable fraction of the major radius, thus being potentially detrimental for fast ion loss (if unstable) as they directly connect core and edge regions. Secondly, the modes tend to have a substantial amplitude even near the plasma edge, at normalized minor radii $\Psi_{pol}^{1/2} \to 1$. Both these features indicate that an external antenna near the plasma edge can couple efficiently to double-gap AEs and be used, for example, as an actuator to affect the fast ion distribution in a controlled way. Finally, although their stability still has to be investigated in detail, modes in class (iii) are arguably strongly stabilized by ion Landau damping, and are not further discussed in this work.

Modes of the type (i)-(ii) show different properties in terms of their radial localization and effective radial width w_{mode}, here defined as

$$w_{mode} \doteq \sum_i |A_i|\, \Delta \Psi_{pol}^{1/2} / A_{max} \qquad (5)$$

where the sum is carried over the (discrete) radial positions used in NOVA. $\Delta \Psi_{pol}^{1/2}$ is the grid points separation, A_i's are the mode amplitude as a function of radius and A_{max} the maximum mode amplitude. Because of the tilt of the TAE gap caused by rotation, TAEs with significant amplitude are mostly localized from mid-radius inward. This corresponds to the location of steepest fast ion gradient (see Fig. 2d), where the fast ion drive is expected to be maximum. For comparable frequencies, EAEs reside in the outboard region of the plasma with respect to TAEs (Fig. 6), where fast ion drive is expected to be small. In fact, modes with EAE character are not commonly observed in NSTX.

Because TAEs are constrained inside a bounded gap, whereas the EAE gap extends outward up to the separatrix, w_{mode} of proper TAE modes slightly decreases for higher toroidal mode numbers because of the effects of rotation on the gap structure. Overall, TAEs feature a narrower radial structure than EAEs as the toroidal mode number increases. However, the coupling to EAE harmonics can substantially alter the effective mode width, see Fig. 8, so that even modes originating in a narrow gap can end up with an effective width of $\simeq 0.3$ (in units of minor radius). These effects are not observed for proper EAEs, whose w_{mode} and gap width are largely independent of n and, generally speaking, broader than for TAEs.

Properties of TAEs and EAEs, along with their possible coupling into double-gap modes, can have important consequences for fast ion transport. Modes of both types, as well as the hybrid double-gap modes, can extend over a significant fraction of the minor radius. Ultimately, the actual impact on fast ion confinement depends on whether these modes (and which ones, among the many ideal eigenmodes obtained through NOVA) are unstable.

V. TAE STABILITY

The NOVA-K kinetic post-processor [12][13] is used to calculate the stability of ideal modes for a given distribution of fast ions, F_{nb}. NOVA-K calculates the TAE drive for a slowing-down distribution in the form [17]

$$F_{nb}(v, \chi) = \frac{F_0}{(v^3 + v_c^3)^{2-\gamma}}\, e^{-\left(\frac{\chi - \chi_0}{\Delta \chi}\right)^2} \qquad (6)$$

where the scaling factor F_0 is a function of the radial position, $\chi = v_\parallel/v$ is the pitch (v is the total fast ion velocity and $v_\parallel$ its projection along the magnetic field) and χ_0 is the pitch at the injection energy, E_0. v_c is the velocity corresponding to the NB critical energy. The coefficient γ defines the slope of the distribution as a function of velocity. The value $\gamma = 1$, corresponding to an ideal slowing-down distribution, is used in this work. The term $\Delta\chi$ defines the broadening of the pitch as a function of velocity for $v < v_0$:

$$\Delta\chi = \Delta\chi_0 - \frac{1}{3} log \left[\frac{(v/v_0)^3 \left[1 + (v_c/v_0)^3 \right]}{(v/v_0)^3 + (v_c/v_0)^3} \right] \quad (7)$$

Here $\Delta\chi_0$ is the broadening in pitch at the injection energy and v_0 the velocity corresponding to E_0.

Equations 6-7 define a single slowing-down distribution, which is usually a poor approximation for plasmas with NB injection. Typical NB systems inject neutrals with at least three distinct energies, including the full energy and components with $1/2$ and $1/3$ of the full energy. In practice, a fit of the the fast ion distribution calculated by the NUBEAM module [18] of the transport code TRANSP [19] is performed with a combination of F_{nb} components, each of which is modeled according to Eqs 6-7. The different components are constrained to have energies in the correct ratio $1 : 1/2 : 1/3$ for each modeled NB source. Sources with different tangency radii have different values for χ_0 and, possibly, for $\Delta\chi_0$. In this study, 6 components are used to model the equivalent of 2 NB sources, each with three energy components. It should be noted that a radial dependence of the parameter χ_0 results from NUBEAM modeling, but it is presently not implemented in NOVA-K. In the following, parameters from the fit calculated at the location of steepest fast ion pressure gradient (typically around $\Psi_{pol}^{1/2} \approx 0.5$) are used as input for NOVA-K.

Once the different F_{nb} components are obtained, a NOVA-K run is performed for each of them. The TAE drive is finally calculated as the sum of the (partial) drive terms from each run. Damping and drive terms are calculated for two NSTX-U scenarios (identifiers $M02$ and $L95$), and compared to the reference NSTX case (identifier $D51$). The NSTX-U scenarios used hereafter are the ones with broadest pressure profile ($M02$) and with the largest fast ion pressure and the steepest radial fast ion profile ($L95$). The remaining NSTX-U case considered previously is expected to have properties in between the NSTX case and those two NSTX-U cases.

Besides the fast ion distribution, plasma rotation is another important factor for TAE stability. Although rotation effects are typically a minor correction for slowly rotating plasmas, they becomes relevant for scenarios where $f_{AE,plasma} \lesssim f_{Doppler}$, such as ST plasmas. As anticipated in the previous Sections, an important limitation of damping rate and drive calculations is that finite rotation is not yet included in a fully consistent way in NOVA. In practice, the ideal MHD solver calculates the Doppler-shifted mode frequencies based on the full
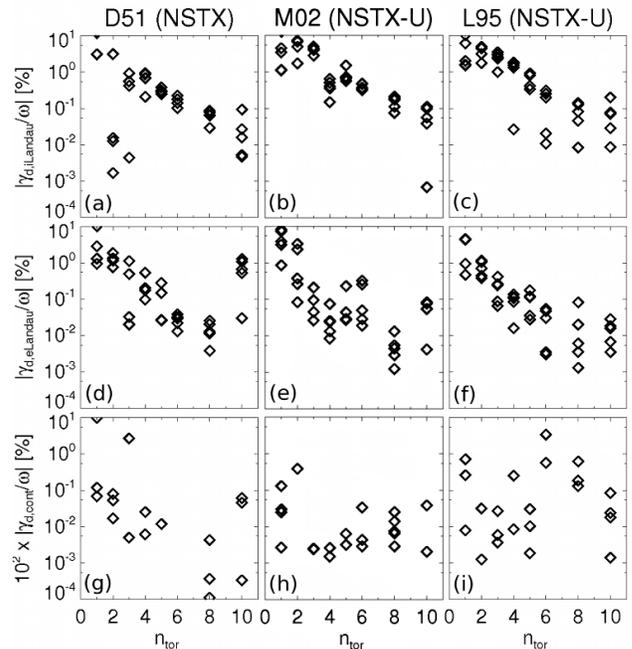

FIG. 9. (Color online) TAE damping rate calculated through NOVA-K for the 5 least stable TAEs with mode number $n = 1 - 10$ for the reference NSTX case $D51$ (left column) and the NSTX-U scenarios $M02$ and $L95$ (center and right columns). Shown are the dominant contributions to the total damping rate from (a-c) ion Landau damping, (d-f) electron Landau damping and (g-i) continuum damping.

rotation profile. Then, only an average rotation value, taken at the mode's peak, is propagated to the kinetic post-processor module to compute the mode stability. A similar approach is used to compute the dominant damping rate term, i.e. ion Landau damping, by replacing the fast ion distribution with a maxwellian with the appropriate thermal ion temperature. With this simplification in mind, the analysis is performed for the same cases shown in Fig. 2 with this approximated treatment of rotation. In the following, linear stability terms are calculated and interpreted in a statistical sense to look for differences and similarities between the reference NSTX case and the predicted NSTX-U scenarios.

A. TAE damping

The first step in the stability comparison is to look at the dominant damping mechanisms, see Fig. 9. When the 5 most unstable (or less stable) modes are included in the analysis, the main difference observed between NSTX and the Upgrade is a general increase of the damping for the Upgrade. Ion Landau damping is the dominant damping mechanism, followed by electron Landau damping which is about a factor 10 weaker. Continuum damping is usually negligible for the modes of interest, for which the interaction with the continuum happens in the
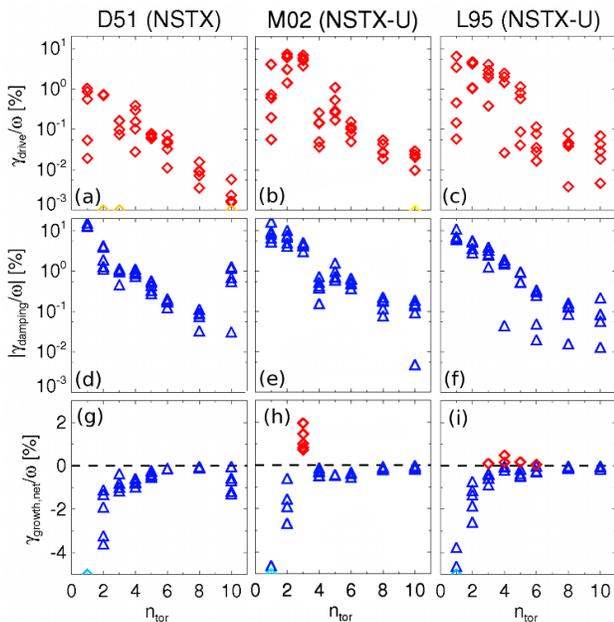
FIG. 10. (Color online) NOVA-K stability results for the 5 least stable TAEs with mode number $n = 1 - 10$ for the reference NSTX case $D51$ (left column) and the NSTX-U scenarios $M02$ and $L95$ (center and right column). Shown are (a-c) the linear drive, (d-f) the total damping and (g-i) the net growth rate. Values outside the plot range are indicated in light colors on the bottom axis.

FIG. 11. (Color online) Critical fast ion β for TAE stability vs. toroidal mode number for the reference NSTX case $D51$ and the NSTX-U scenarios $M02$ and $L95$. Dashed lines indicate the actual β values for the three cases.

low shear region. Since ion temperature is only $\approx 50\%$ higher in the NSTX-U cases, it appears that the increase in density is the main factor leading to a larger ion Landau damping. A dependence of the Landau damping terms on the toroidal mode number is observed. The stronger damping is computed for low-n modes, $n \lesssim 4$. A plateau is then reached for $n \gtrsim 6$. Overall, no clear differences are observed for the NSTX-U scenarios characterized by various combinations of NB injection sources, so that damping plays a similar role for all cases in determining the overall TAE stability.

It should be noted that the validity of the NOVA-K formulation for other damping mechanisms, such as radiative damping [20], is arguable in the limit of small aspect ratio, and they are neglected in this work.

B. TAE drive

The next piece of information to project AE stability to NSTX-U is provided by the fast ion distribution, as calculated by NUBEAM. The radial fast ion pressure profiles are shown in Fig. 2c, from which it is clear that the higher field and the larger electron temperature (i.e. longer slowing-down time) on NSTX-U imply higher fast ion pressures on NSTX-U. The peaking factor depends strongly on the specific combination of NB sources, with very peaked profiles when the NB source with $R_{tan} = 110$
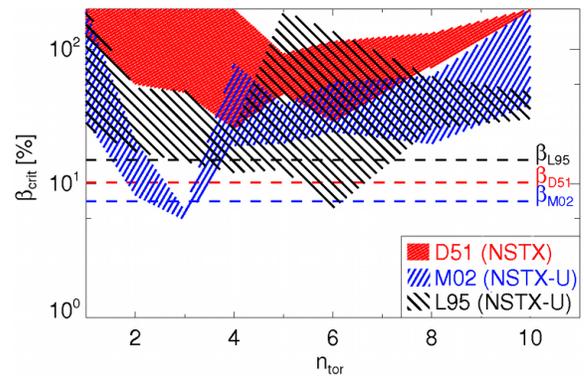
cm is used (case $L95$) and a broader profile as the tangency radius of the second NB line is shifted toward the outer plasma region (case $M02$).

Both the improved confinement (i.e. larger fast ion β) and the potentially more peaked radial profile combine to enhance the AE growth rate for NSTX-U scenarios. This is shown in Fig. 10, where the AE drive and net growth rate are compared for the NSTX reference case and for the NSTX-U scenarios exhibiting the largest fast ion pressure and the broader pressure profile. Overall, the NSTX-U projected scenario features a larger drive for TAEs. Contrary to the NSTX case, *unstable* TAEs are found. For instance, the larger fast ion β alone results in unstable $n = 3$ TAEs for the broad pressure case (Fig. 10h). The spectrum of unstable modes is further expanded for more peaked profiles (Fig. 10i), resulting in unstable TAEs for $3 < n < 7$, although the net growth rate is still quite small, $\gamma_{growth,net}/\omega \lesssim 1\%$.

A summary of the stability analysis is shown in Fig. 11 in terms of *critical fast ion* β, β_{crit}. The latter is defined as the minimum fast ion β required to bring modes to marginal stability, where drive and damping equal each other. The trend that emerges from Fig. 11 is that β_{crit} is generally lower for NSTX-U scenarios, implying a more efficient drive, and mode instability can be further enhanced by the larger fast ion β.

Another element of the increased fast ion drive for TAEs is illustrated in Fig. 12, in which the TAE drive contributions are shown separately for each NB energy component. Fast ions closer to the injection energy, which represent the main contribution to the total fast ion β, provide $\approx 70\%$ or more of the total drive for NSTX-U scenarios, with the remaining $\lesssim 30\%$ coming from the $E_{inj}/2$ component and a negligible (or even *stabilizing*) role of the lower energy fast ions. Conversely, the higher energy ions contribution to TAE drive is $50 - 60\%$ for the NSTX case, which is comparable to (or only slightly less than) the sum of contributions from the $E_{inj}/2$ and $E_{inj}/3$ energy components. The increased TAE instabil-
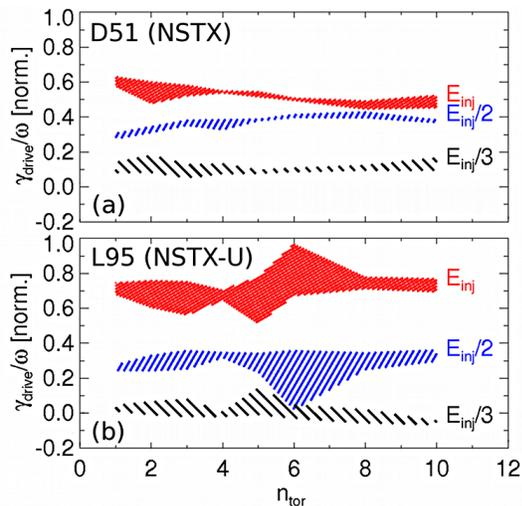
FIG. 12. (Color online) Relative contributions to the total TAE drive from the three energy components (full, 1/2 and 1/3 of the NB injection energy) for (a) the reference NSTX case $D51$ and (b) the NSTX-U scenario $L95$.
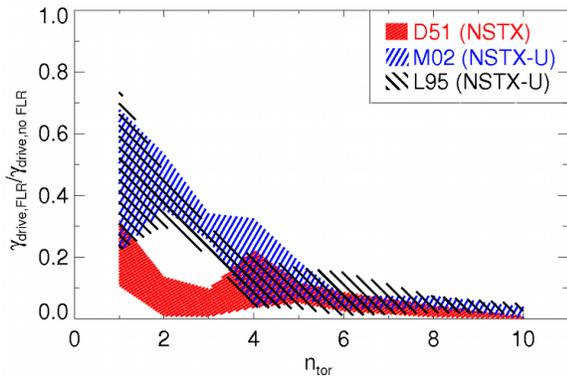

FIG. 13. (Color online) Finite Larmor radius effects on the total TAE drive. Note the reduced FLR stabilization at $n \lesssim 5$ for the two NSTX-U scenarios.

ity for NSTX-U scenarios is further exacerbated by the reduction of finite Larmor radius (FLR) effects on mode stabilization [13]. Figure 13 presents the ratio of TAE drive with FLR effects over the drive without FLR effects, $\gamma_{drive}/\gamma_{drive,noFLR}$. For the NSTX case, the ratio is consistently $\lesssim 20\%$, indicating a reduction by more than a factor 5 in the calculated drive once FLR effects are accounted for. Instead, larger values of $\gamma_{drive}/\gamma_{drive,noFLR}$ are obtained for both NSTX-U scenario. FLR stabilization is especially important for $n \lesssim 5$, when the enhanced drive can possibly overcome the total damping (cf. Figs. 10d-f) and result in unstable TAE modes.

In addition to the larger fast ion pressure (or β) and FLR effects, the more tangential injection geometry of the new NB lines of NSTX-U is also responsible for the increased TAE drive. The new NB sources (and especially the one with tangency radius $R_{tan} = 110$ cm, near the magnetic axis) inject particles with pitch closer to
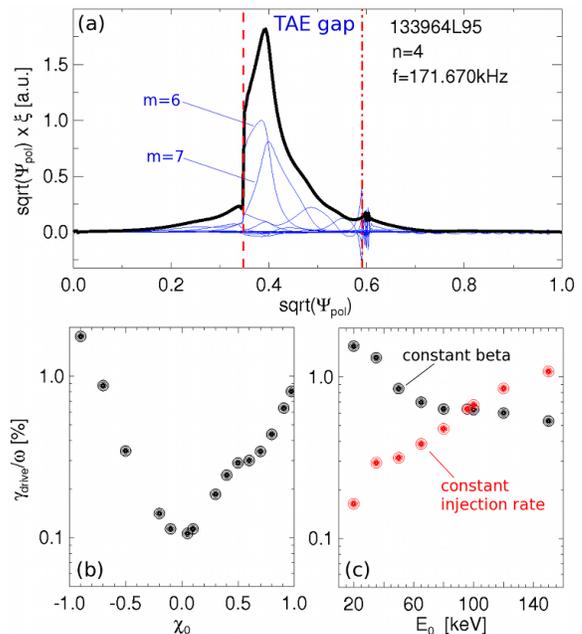

FIG. 14. (Color online) Trend of TAE stability for a $n = 4$ mode, shown in panel (a) with the dominant $m = 6, 7$ poloidal harmonics marked, vs. (b) fast ion pitch and (c) NB injection energy. In (c) data in black assume the same fast ion $\beta = 7.6\%$, data in red assume constant NB injection rate.

$\chi \approx 1$. The resulting large fraction of strongly co-passing fast ions populates a region of phase space with numerous TAE resonances, hence the large TAE drive. Figure 14 illustrates the dependence of the drive for a $n = 4$ TAE as a function of the injection pitch, χ_0, and of the injection energy, E_0. For the example in Fig. 14b, a single slowing down distribution with $E_0 = 90$ keV and varying χ_0 is used. A more than tenfold increase in the TAE growth rate is observed as χ_0 is varied from 0 (corresponding to perpendicular NB injection) to 1 (tangential injection). A similar increase is also obtained for an hypothetical counter-NB injection with $\chi_0 < 0$. A more modest increase of γ_{drive}/ω is observed as the injection energy is decreased down to 20 keV at constant fast ion β, see Fig. 14c. This suggests that lower energy fast ions, with velocity approaching the Alfvén velocity, might be more efficient to drive the modes than particles near the injection energy, see Fig. 16 below. However, it should be noted that the results at constant fast ion β are only indicative of the relative efficiency of fast ion populations at different energies to drive the modes. In real experiments with NB auxiliary systems, β would be reduced as the energy is decreased and the NB injection rate is maintained nearly constant. In that case, a net *decrease* of the TAE drive at lower energies is observed (consistent with the results shown in Fig. 12).

The role of strongly co-passing particles in driving TAEs is confirmed by using the ORBIT particle following code [21] to identify wave-particle resonances for the TAE mode shown in Fig. 14a. A test distribution of fast ions is
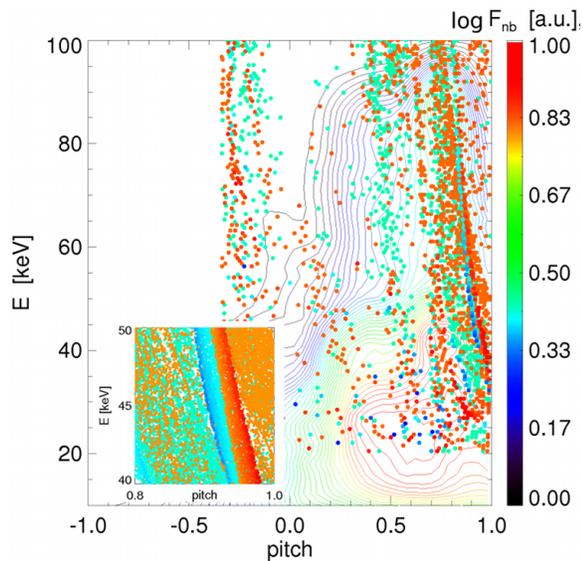
FIG. 15. (Color online) Fast ion distribution at $\Psi_{pol}^{1/2} = 0.5$. The dots show the location of resonances, computed through ORBIT, for the $n = 4$ TAE mode in Fig. 14a. The simulation is restricted to energies $20-100$ keV. Peak mode amplitude is $\delta B/B \sim 10^{-4}$. Particles that gain (lose) energy because of the resonant interaction are shown in red (blue). The inset shows an expanded view with increased resolution of the region with $E = 40-50$ keV and pitch $\chi \geq 0.8$ to illustrate the abundance of potential resonances.

FIG. 16. (Color online) Main resonances in the P_ζ, μ space for the $n = 4$ mode shown in Fig. 14a, calculated for mono-energetic fast ion distributions with (a) $E_0 = 30$ keV and (b) $E_0 = 90$ keV. Ψ_w is the value of poloidal flux at the separatrix, B_0 the magnetic field on axis. Color coding is the same as in Fig. 15. The different phase space domains [24] are marked in panel (a) and correspond to the following orbit types: (1) co-passing, (2) counter-passing, (3) trapped, (4) potato, (5) stagnation, (6) lost counter-passing and trapped and (7) lost co-passing.

used to fill in the whole phase space. Then, ORBIT computes the guiding center orbits in the presence of MHD perturbations with a given frequency and wavenumber spectrum. To identify resonances, the orbit of pairs of particles with equal energy E and magnetic moment μ, but slightly different toroidal canonical momentum P_ζ, is followed. Their relative angle in the P_ζ, θ plane (the latter being the poloidal angle) is recorded during the simulation. The angle varies by 2π over a trapping bounce time for resonant particles, which provides a criterion to unambiguously identify the resonance. (More details on the method are given in Refs. [22]-[23]).

The results from ORBIT simulations shown in Fig. 15 confirm that resonances are mostly located at values $\chi \gtrsim 0.7$. According to TRANSP, this is a region that is densely populated by the NSTX-U neutral beams. Therefore, a decreasing number of particles will contribute to the TAE drive as the injection pitch χ_0 is decreased toward smaller values, which is consistent with the curve from NOVA-K in Fig. 14b.

Similar results are obtained over the the entire radial range over which the TAE modes have finite amplitude. This is illustrated in Fig. 16, where two mono-energetic populations with $E_0 = 30$ keV and $E_0 = 90$ keV are used in ORBIT to sample the entire P_ζ, μ space. Since P_ζ is correlated with the radial coordinate [24], this corresponds to sampling all radial positions. The scan in μ implies that particles belonging to all possible classes
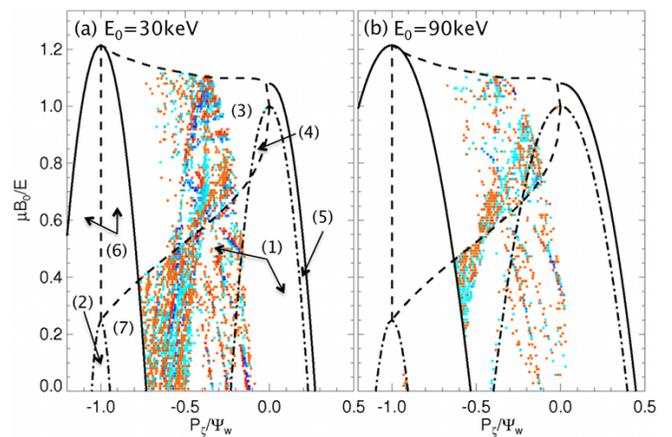
(e.g. co-passing, counter-passing, trapped, etc.) are included. Consistently with what shown in Fig. 15, a large number of resonances are identified over a broad portion of phase space, in spite of the fact that a relatively small mode amplitude, with peak values $\delta B/B \sim 10^{-4}$, is used.

Much broader resonances would appear for amplitudes that correspond, for instance, to so-called TAE *avalanche* events [7][8][11]. The scaling of resonance width with mode amplitude is shown in Fig. 17 for particles with $E_0 = 90$ keV and $\chi = 0.9$. Test particles are initialized over the entire minor radius to obtain a so-called *kinetic Poincarè plot* [24]. Besides the large number of islands forming in the θ, $\Psi_{pol}^{1/2}$ plane even for a single value of energy and pitch, the increase in number and size of the resonances can be readily seen by comparing Figs. 17a-b. It should be noted that resonance width is a crucial parameter to define the transition into a regime where strong departure from the mode's linear properties, interaction between multiple modes or stochastization of phase space can lead to an enhancement of fast ion transport [11][25][26]. The transition to a strongly non-linear regime is believed to happen during TAE avalanches, and the possibility that events of this type may occur on NSTX-U should not be ruled out.

VI. SUMMARY AND CONCLUSIONS

Initial calculations of the general properties of Alfvènic modes in the TAE range of frequency have been performed for different NSTX-U scenarios and compared
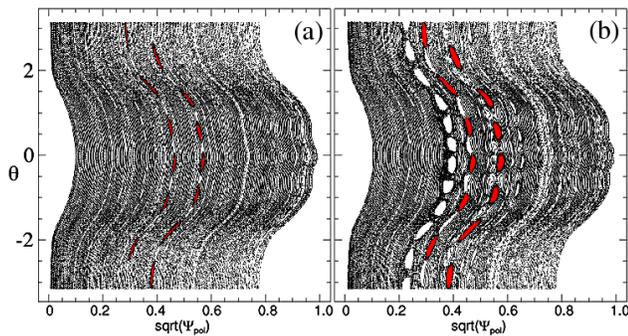
FIG. 17. (Color online) Kinetic Poincarè plot in the θ, $\Psi_{pol}^{1/2}$ plane showing resonances for the $n = 4$ mode shown in Fig. 14a. Particles are initialized with $E_0 = 90$ keV and and $\chi_0 \simeq 0.9$. Panels (a)-(b) correspond to a peak mode amplitude $\delta B/B \sim 10^{-4}$ and $\delta B/B \sim 10^{-3}$, respectively. Some of the resonances, appearing as *islands* in the Poincarè plot, are highlighted in red.

to a baseline NSTX scenario. NSTX-U cases feature a toroidal magnetic field $B_t \approx 0.8$ T, that is the maximum value expected during the initial year of NSTX-U operation. Cases with different NB injection geometries, among the choices that will be available on NSTX-U, have been considered.

Overall, general properties of TAE and EAE modes scale according to simple formulas for the gap frequency and width. Because of the higher magnetic field, the mode frequency is expected to nearly double with respect to NSTX. The spectrum of most unstable modes is projected to be in the range $n = 2 - 10$, which is broader than what observed on NSTX.

The upshift in frequency and toroidal mode number, coupled to a large toroidal plasma rotation, is expected to determine a reduction in the radial width of the TAE gap, hence of the unstable modes. However, this effect may be counter-acted by the occurrence of *double-gap* modes, which feature broader mode structures as a result

of coupling between TAE and EAE modes.

The stability of TAE modes has been investigated through the NOVA-K code. Plasma rotation is included in a simplified form. Nevertheless, the general conclusions, as well as the trend with respect to NSTX scenarios, are believed to be valid.

The main damping mechanism for the modes under consideration is identified as ion Landau damping, followed by electron Landau damping and continuum damping in order of importance. Overall, damping rates are found to increase for the denser, hotter NSTX-U plasmas with respect to NSTX plasmas.

Although damping rates increase, the TAE drive is also enhanced in NSTX-U because of the larger fast ion pressure and reduced FLR stabilization effects. The use of NB sources with nearly tangential injection further increases the drive by populating regions of phase space where numerous resonances are present. The quantitative aspects of mode stability discussed in Sec. V depend on the specific TAE mode under consideration. Nevertheless, the qualitative conclusions are expected to be valid for most of the AE modes considered in this study, namely TAEs (and, indirectly, RSAEs) and EAEs.

Further upgrades of the NOVA-K code are under consideration for improved analysis and prediction capability. Improvements will address two main issues of the present code version, namely the lack of fully consistent treatment of rotation in the stability calculations and the simplified description of the fast ion distribution, F_{nb}. Future studies will include the dependence of AE properties and stability on NSTX-U upon parameters not considered in this work, such as q-profile (including reverse-shear scenarios), plasma density and temperature.

[1] M. Ono, S. M. Kaye, Y.-K. M. Peng, G. Barnes, W. Blanchard, M. D. Carter, J. Chrzanowski, L. Dudek, R. Ewig, D. Gates, R. E. Hatcher, T. Jarboe, S. C. Jardin, D. Johnson, R. Kaita, M. Kalish, C. E. Kessel, H. Kugel, R. Maingi, R. Majeski, J. Manickam, B. Mc-Cormack, J. Menard, D. Mueller, B. Nelson, B. Nelson, C. Neumeyer, G. Oliaro, F. Paoletti, R. Parsells, E. Perry, N. Pomphrey, S. Ramakrishnan, R. Raman, G. Rewoldt, J. Robinson, A. L. Roquemore, P. Ryan, S. Sabbagh, D. Swain, E. J. Synakowski, M. Viola, M. Williams, J. R. Wilson, and NSTX Team, Nucl. Fusion **40**, 557 (2000).

[2] J. E. Menard, S. Gerhardt, M. Bell, J. Bialek, A. Brooks, J. Canik, J. Chrzanowski, M. Denault, L. Dudek, D. A. Gates, N. Gorelenkov, W. Guttenfelder, R. Hatcher, J. Hosea, R. Kaita, S. Kaye, C. Kessel, E. Kolemen,

H. Kugel, R. Maingi, M. Mardenfeld, D. Mueller, B. Nelson, C. Neumeyer, M. Ono, E. Perry, R. Ramakrishnan, R. Raman, Y. Ren, S. Sabbagh, M. Smith, V. Soukhanovskii, T. Stevenson, R. Strykowsky, D. Stutman, G. Taylor, P. Titus, K. Tresemer, K. Tritz, M. Viola, M. Williams, R. Woolley, H. Yuh, H. Zhang, Y. Zhai, A. Zolfaghari, and NSTX Team, Nucl. Fusion **52**, 083015 (2012).

[3] J. E. Menard, T. Brown, J. Canik, J. Chrzanowski, L. Dudek, L. El Guebaly, S. Gerhardt, S. Kaye, C. Kessel, E. Kolemen, M. Kotschenreuther, R. Maingi, C. Neumeyer, M. Ono, R. Raman, S. Sabbagh, V. Soukhanovskii, T. Stevenson, R. Strykowsky, P. Titus, P. Valanju, G. Voss, A. Zolfaghari, and NSTX Upgrade Team, in Proceedings of the 24th IAEA-FEC meeting, FTP/3-4

(San Diego, California, USA, 2012).

[4] A. Fasoli, C. Gormezano, H. L. Berk, B. N. Breizman, S. Briguglio, D. S. Darrow, N. N. Gorelenkov, W. W. Heidbrink, A. Jaun, S. V. Konovalov, R. Nazikian, J.-M. Noterdaeme, S. Sharapov, K. Shinoara, D. Testa, K. Tobita, Y. Todo, G. Vlad, and F. Zonca, Nucl. Fusion **47**, S264 (2007).

[5] W. W. Heidbrink, Phys. Plasmas **15**, 055501 (2008).

[6] S. S. Medley, N. N. Gorelenkov, R. Andre, R. E. Bell, D. S. Darrow, E. D. Fredrickson, S. M. Kaye, B. P. LeBlanc, A. L. Roquemore, and NSTX team, Nucl. Fusion **44**, 1158 (2004).

[7] M. Podestà, W. W. Heidbrink, D. Liu, E. Ruskov, R. E. Bell, D. S. Darrow, E. D. Fredrickson, N. N. Gorelenkov, G. J. Kramer, B. P. LeBlanc, S. S. Medley, A. L. Roquemore, N. A. Crocker, S. Kubota, and H. Yuh, Phys. Plasmas **16**, 056104 (2009).

[8] E. D. Fredrickson, N. A. Crocker, R. E. Bell, D. S. Darrow, N. N. Gorelenkov, G. J. Kramer, S. Kubota, F. M. Levinton, D. Liu, S. S. Medley, M. Podestà, K. Tritz, R. B. White, and H. Yuh, Phys. Plasmas **16**, 122505 (2009).

[9] E. D. Fredrickson, N. A. Crocker, D. S. Darrow, N. N. Gorelenkov, G. J. Kramer, S. Kubota, M. Podestà, R. B. White, A. Bortolon, S. P. Gerhardt, R. E. Bell, A. Diallo, B. P. LeBlanc, F. M. Levinton, and H. Yuh, Nucl. Fusion **53**, 013006 (2013).

[10] S. P. Gerhardt, E. Fredrickson, D. Gates, S. Kaye, J. Menard, M. G. Bell, R. E. Bell, B. P. LeBlanc, H. Kugel, S. A. Sabbagh, and H. Yuh, Nucl. Fusion **51**, 033004 (2011).

[11] D. S. Darrow, N. Crocker, E. D. Fredrickson, N. N.

Gorelenkov, M. Gorelenkova, S. Kubota, S. S. Medley, M. Podestà, L. Shi, and R. B. White, Nucl. Fusion **53**, 013009 (2013).

[12] C. Z. Cheng, Phys. Rep. 211 **1** (1992).

[13] N. N. Gorelenkov, C. Z. Cheng, and G. Y. Fu, Phys. Plasmas **6**, 2802 (1999).

[14] S. P. Gerhardt, R. Andre, and J. E. Menard, Nucl. Fusion **52**, 083020 (2012).

[15] G. Y. Fu and C. Z. Cheng, Phys. Fluids B **4**, 3722 (1992).

[16] N. N. Gorelenkov, Phys. Rev. Lett. **95**, 265003 (2005).

[17] N. N. Gorelenkov, H. L. Berk, and R. V. Budny, Nucl. Fusion **45**, 226 (2005).

[18] A. Pankin and D. McCune and R. Andre and G. Bateman and A. Kritz, Computer Physics Communication **159**, 157 (2004).

[19] `http://w3.pppl.gov/transp/`.

[20] H. L. Berk, R. R. Mett, and D. M. Lindberg, Phys. Fluids B **5**, 3969 (1993).

[21] R. B. White and M. S. Chance, Phys. Fluids **27**, 2455 (1984).

[22] R. B. White, Plasma Phys. Control. Fusion **53**, 085018 (2011).

[23] R. B. White, Commun. Nonlinear Sci. Numer. Simulat. **17**, 2200 (2012).

[24] R. B. White, The theory of toroidally confined plasmas, 2nd ed. (Imperial College Press, London, UK, 2006).

[25] M. Schneller, P. Lauber, M. Brüdgam, S. D. Pinches, and S. Günter, Nucl. Fusion **52**, 103019 (2012).

[26] R. B. White, N. N. Gorelenkov, W. W. Heidbrink, and M. A. V. Zeeland, Plasma Phys. Control. Fusion **52**, 045012 (2010).

Information Services
Princeton Plasma Physics Laboratory
P.O. Box 451
Princeton, NJ 08543

Phone: 609-243-2245
Fax: 609-243-2751
e-mail: pppl_info@pppl.gov
Internet Address: http://www.pppl.gov